A&A manuscript no.
(will be inserted by hand later)

Your thesaurus codes are:
03(03.01.2;03.19.1;03.20.2)

ASTRONOMY
AND
ASTROPHYSICS
21.11.1995

The ESO Atmospheric Temporal Coherence Monitor Dedicated to High Angular Resolution Imaging

Bruno Lopez[1] **and Marc Sarazin**[2]

[1] O.C.A Dpt. Fresnel - URA CNRS 1361 B.P. 229 - F-06304 Nice Cedex 4
[2] European Southern Observatory, Karl-Schwarzschild Str. 2, D-8046 Garching bei München, F.R.G.

November 21, 1995

Abstract. Seeing monitors using the differential image motion method were developed in the eighties for several site studies worldwide. Such an instrument has been included in the Astronomical Weather Station of La Silla, now part of standard astronomical observing in the observatory. In preparation for the interferometric mode of the VLT at Cerro Paranal, a new type of measurement has been undertaken to understand the physics of atmospheric motion and its relation to the temporal coherence of the wavefront at the telescope level. The concept of the coherence monitor is described and the first results of continuous monitoring with a prototype instrument are presented.

Key words: Interferometry, Seeing, Earth atmospheric motion

1. Introduction

The development of high resolution imaging techniques require constant improvement of the operational tools. In particular, the performance of observations made by interferometry is extremely dependent on the quality of atmospheric seeing. A monitoring of the relevant atmospheric parameters is therefore essential.

The signal to noise ratio for long baseline interferometry (Roddier & Lena 1984) is related to the Fried parameter r_0 at least with a third power law and is proportional to the exposure time τ. The longest permissible or equivalently, the optimum exposure time which determines the depth of the recorded images, is limited by the degree of coherence of the turbulent atmosphere. That is to say the integration time has to be short enough to preserve the high spatial frequency content of the observed signal otherwise blurred by the wavefront corrugation.

While r_0 statistics are nowadays better understood, we still have a poor quantitative knowledge of the wavefront temporal coherence which was monitored only for a few nights over various sites (Scaddan & Walker 1978, Aime et al. 1986, Vernin et al. 1991). It is an independent random parameter without any systematic correlation with the Fried quantity. Due to its large expected variance, the optimum exposure time has a significant weight in the instantaneous signal to noise ratio in spite of its weak power dependency.

Whatever the way to observe (Adaptive Optics, Long Baseline Interferometry or Speckle Interferometry), the optimum exposure time is related to the horizontal motion of the turbulent atmosphere (§ 2.2). The Differential Image Motion Method (DIMM) summarized in § 3 has proven its efficiency for the monitoring of r_0 (Fried 1975, Sarazin & Roddier 1990). A method based on the temporal correlation of image motion had been previously proposed for the qualitative study of τ (Müller et al. 1988, Abitbol et al. 1991). Here, this paper presents another simple and promising method recently tested at ESO observatories to obtain quantitative estimates of this parameter.

The DIMM principle is again used but a new theory based on the analysis of the velocity of image motion instead of temporal correlation leads to the statistical measure of the velocity of the turbulent layers as shown in § 4. The ESO seeing monitors have been adapted to this purpose. The necessary instrumental modifications consist in the use of a scanning mirror which increases the individual image acquisition rate up to 500 Hz (§ 4.2). First results of monitoring made at La Silla are presented in § 5.

Scientifically, a better understanding of site behavior for high resolution imaging will be achieved. Moreover the parallel monitoring of τ will improve the strategy of observation in interferometry, permitting to adapt astronomical programs, in particular for faint sources, to the chaotic nature of the Earth's atmosphere.

Send offprint requests to: Bruno Lopez

2. Physics of the wavefront temporal characteristics.

2.1. Mechanism of turbulence induction, Fried parameter

Under typical astronomical conditions, the random spatial variations of the index of refraction of air depends mainly on temperature fluctuations through the Earth's atmosphere. The effect of water vapor and pressure variations is generally small enough to be ignored. Because of the low kinematic viscosity of air, the Reynolds number of the atmosphere in motion always exceeds its critical value which allows for well developed mechanical turbulence. The mixing between warm and cold air masses therefore creates inhomogeneities of the tempera-

ture field, responsible for the phase perturbations detected on a wavefront propagating through it.
The Kolmogorov model which applies for fluid turbulence is commonly used to describe, statistically, spatial structures of the atmosphere. It assumes that the kinetic energy, contained in a turbulent flow, is transferred without any loss from the largest eddies to the smallest ones, until being finally dissipated by viscosity. The phase shift φ of the corrugation is usually given in terms of structure functions :

$$\begin{aligned} D_\varphi(r) &= <\mid \varphi(x)-\varphi(x-r)\mid^2> \\ &= 2.91\left(\frac{2\pi}{\lambda}\right)^2 \int_0^H C_n^2\,(h)\,dh\, r^{5/3} \end{aligned} \quad (1)$$

where the scintillation phenomenon on the wavefront has been neglected under the assumption called the near field approximation. The subscript of D implies that the random variable is the received phase field. x and r are lengths in the horizontal plane. The 5/3 power law results from the Kolmogorov cascade, λ is the wavelength. The structure coefficient $C_n^2(h)$, which depends on altitude, relates to the amount of refractive index fluctuations affecting optical propagation. As the phase shift of the perturbations is caused by several regions of turbulence over the atmospheric column, the structure function at ground level is related to the integral of $C_n^2(h)$. This equation is valid in the inertial range, bounded by the inner scale of turbulence l_0, at which viscous dissipation arises, and by the outer scale L_0 or equivalently the size of the largest eddies maintaining isotropic properties.
One very convenient quantity, outlined by Fried, is the critical pupil diameter r_0 under which the resolving power of a telescope is diffraction limited. Above this value, seeing effects linked to the turbulent atmosphere seriously affect image quality. The Fried parameter r_0 is equally defined as the diameter of the mean area of optical coherence on the wavefront, within which the mean square phase variations are less than $1\,rd^2$:

$$r_0 = \left[0.423\left(\frac{2\pi}{\lambda}\right)\int C_n^2(h)dh\right]^{-3/5} \quad (2)$$

2.2. Wavefront temporal characteristics

In astronomy, high resolution imagery implies both a high signal level in the recorded image and short enough exposures for a correct signal sampling. A major constraint is therefore imposed by the time variations of wavefront perturbations (or coherence time for the atmosphere). The coherence length r_0, as given by Fried, is a statistical parameter which does not invoke any temporal change. In a simplified model, the temporal change is attributed to the horizontal motion of a frozen atmosphere, acting as a single moving phase screen. The shift of equally frozen phase corrugation moves therefore at the mean wind velocity and in the mean wind direction. This assumption named the Taylor hypothesis allows to define the coherence time of the kinematic atmosphere using the simple equation,

$$\tau = \frac{r_0}{v} \quad (3)$$

where τ is clearly the time required to pass over an area of coherence r_0.
In fact, to be consistent with reality, several moving turbulent layers must be considered. In particular, the case of speckle interferometry illustrates the inadequacy of the Taylor model: considering ad absurdum a telescope of infinite diameter, the speckle pattern observed would not be affected by the motion of a single frozen atmospheric layer. It is the dispersion velocity among different layers which induces a phase corrugation change on the wavefront, and consequently onto the speckle pattern. The multiple atmospheric layers model illustrated in Fig. 1 provides a more realistic picture in which the motion of speckles is characterized by the speckle life time (or speckle boiling time) following Roddier et al. 1982:

$$\tau = \frac{r_0}{\overline{\Delta v}} \quad (4)$$

with Δv, the average dispersion velocity, given by:

$$\overline{\Delta v} = \left[\frac{\int_0^\infty \mid v(h)\mid^2\, C_n^2(h)dh}{\int_0^\infty C_n^2\,(h)\,dh} - \left|\frac{\int_0^\infty v(h)C_n^2(h)\,dh}{\int_0^\infty C_n^2\,(h)dh}\right|^2\right]^{1/2} \quad (5)$$

where $v(h)$ is the wind velocity at altitude h.

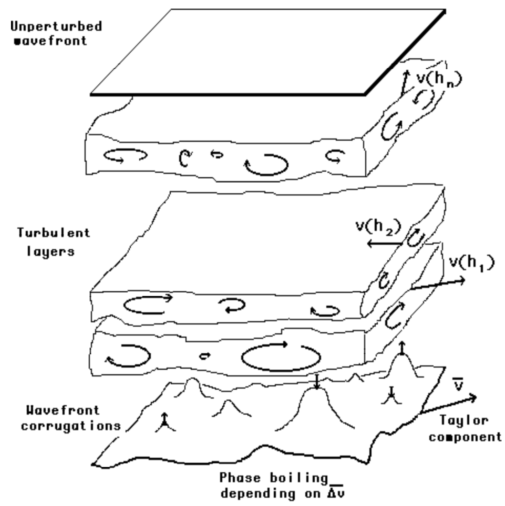

Fig. 1. The kinematic model of multiple and thin atmospheric layers moving independently of one another.

For the Michelson interferometry case, to which the adaptive optic technique and the long baseline interferometry belong, the relation between the turbulent atmosphere and the optimum response time or exposure time for fringe pattern is again different. The transit time of perturbations over the telescope pupil determines the coherence time τ for Milchelson interferometry:

$$\tau = \frac{r_0}{v^*} \quad (6)$$

which now depends on a mean characteristic velocity of the turbulent layers v^* defined as:

$$v^* = \left[\frac{\int_0^\infty \mid v(h)\mid^{5/3}\, C_n^2(h)\,dh}{\int_0^\infty C_n^2(h)\,dh}\right]^{3/5} \quad (7)$$

Michelson interferometry is in fact a complex field which should be subdivided into specific modes in order to obtain more accurate relationships. One of them is long baseline interferometry where the outer scale of turbulence has some influence on the lifetime of the interference fringes.
Consequently, for a model of atmosphere constituted by multiple turbulent layers, each observing mode has its own requirement summarized in Table 1, being either the longest permissible exposure time or, as for adaptive optics, the response time which is best adapted to the evolution of wavefront corrugation.

Table 1. Main temporal coherence parameter of high resolution imaging modes.

Observing mode	Atmospheric parameter
Speckle Interferometry	$r_0 \,/\, \Delta v$
Adaptive Optics	$r_0 \,/\, v^*$
Michelson Interferometry	$r_0 \,/\, v^*$

3. Description of the differential motion monitor

3.1. Classical differential image motion monitor operation

The presence of turbulence in the Earth's atmosphere causes the stellar image formed by a telescope of small diameter to move randomly. The position of the stellar image in the focal plane is directly related to the tilt angle of the wavefront with regard to the entrance pupil plane of the telescope. According to theoretical calculations, the atmospheric turbulence can be estimated through the variance of the image motion. In practice, in order to measure accurately a rough mean square angle of arrival of the order of 0.1 arcsec^2 it is necessary to avoid any side-effect due to tracking errors of the telescope. For this purpose, (Fried 1975) suggested to use the differential motion method where two separated apertures are used to form two different images of the same star. The differential motion of these images is then analyzed instead of their absolute motion. The formalism of the theory has been analytically described by (Roddier 1981). Two structure functions for the angle of arrival of light α are derived in the directions parallel and perpendicular to the subpupil separation:

$$D_{\alpha,\parallel} = 2\lambda^2\, r_0^{-5/3}(0.179\, D^{-1/3} - 0.0968\, d^{-1/3}) \quad (8)$$

$$D_{\alpha,\perp} = 2\lambda^2\, r_0^{-5/3}(0.179\, D^{-1/3} - 0.145\, d^{-1/3}) \quad (9)$$

where D is the subpupils diameter and d their separation center to center.
Assuming that the turbulence characteristics is stationary, the structure functions are determined through a set of measures of wavefront slope differences. The Fried parameter r_0 is then deduced from the above relations.

3.2. DIMM System description

The differential image motion method has been extensively used at ESO to predict the quality of the image an astronomical large telescope would produce. Long term surveys of seeing conditions were performed, particularly for the search for the observatory site for the European Very Large Telescope.

The theory of differential motion is reviewed in (Sarazin & Roddier 1990), along with a description of the seeing monitor instruments in use since 1987. The seeing monitors are Cassegrain telescopes of 35 cm diameter. The entrance pupil is re-imaged behind the Cassegrain focus by means of a Fabry lens. To obtain dual star images, whose relative motion in the image plane represent local wavefront tilt differences, a pupil mask associated with a roof prism is installed in the conjugate of the entrance pupil plane taken at the primary mirror level. The subpupils are realized by two holes in the pupil mask. As the prism splits the two beams, two separate images of the star are further formed in the image plane. The detector used is a microchannel plate image inverter intensifier tube on a 576x384 frame transfer CCD. Each stellar image covers an area of at least 3x3 pixels with a pixel angular size of 0.88 arcsec. The uncertainty in the determination of the relative positions of the image centroids corresponds to a noise of variance N_α^2:

$$N_\alpha^2 = 0.01 \pm 0.002\, pixel^2 \quad (10)$$

as measured in the laboratory for circular images. An electromagnetic shutter is used to obtain 10 ms exposure time per frame which is most of the time short enough to freeze the turbulence effects. Data reduction is made in real time after 200 differential image positions are sampled and leads to one r_0 estimate every 2 minutes.

4. Description of the coherence monitor

4.1. Velocity of differential motion

The differential image motion principle is a practical means for an experimental diagnosis of the temporal dependence of the atmospheric effects on either speckle interferometry or Michelson interferometry. Indeed, the analysis of the velocity of the wavefront slope or, in other words, of the differential image motion velocity at the focus of a small telescope, contains the necessary statistical information on the velocity of the turbulent layers (Lopez & Sarazin 1991). The optimum exposure times, defined in § 2, which are linked to the vertical distribution of wind and turbulence in the atmosphere can then be derived.
The new method consists of extending the differential image motion theory to a kinematic model for the atmosphere. The study of the tilt velocity rather than of the tilt amplitude only leads then to the following structure function along any direction of the pupil plane making an angle γ with the subpupil separation axis (Lopez 1992):

$$D_{\frac{\partial\alpha}{\partial t},\gamma} = 2 \cdot 0.128\lambda^2 r_0^{-5/3} D^{-7/3} \cdot \left(\overline{v}^2(1+2\cos^2(\theta-\gamma)) + 2\overline{\Delta v}^2\right)\left(1 - f(\overline{v},\theta,\overline{\Delta v},D,d,\gamma)\right) \quad (11)$$

The quantities $\overline{v}$, θ and $\overline{\Delta v}$ provide the statistical measure of the velocity patterns of the turbulent atmosphere:

- $\overline{\Delta v}$ is the same dispersion velocity as the one defined in Eq. (5). The speckle boiling time is inversely proportional to this value.
- $\overline{v}$ is the averaged velocity of the turbulent layers:

$$\overline{v} = \frac{\int_0^H v(h)\, C_n^2(h) dh}{\int_0^H C_n^2(h) dh} \quad (12)$$

The parameter $\overline{v}$, together with $\overline{\Delta v}$ determine boundaries for v^* (Appendix 1) which is directly related to the optimum response time for adaptive optics and for Michelson interferometry as a whole.

– θ is the angle made between the subpupil direction and the mean direction of displacement of the turbulent layers. It is, in the Taylor sense, the main direction of motion of the wavefront corrugations. This parameter may be used in relation with recent work (Jorgenson et al. 1991) using the chaotic behavior of the turbulence to predict the wavefront evolution, thus increasing the efficiency of active correction systems.

In the Eq. (12), $f(\overline{v}, \theta, \overline{\Delta v}, D, d, \gamma)$ is the covariance factor for the tilt velocity in front of the two subapertures. It may be computed as follows:

$$f(\overline{v},\, \theta, \overline{\Delta v},\, D,\, d,\, \gamma) = \tag{13}$$
$$\left(\frac{\overline{v}^2\, \cos^2(\theta-\gamma)+\frac{1}{2}\overline{\Delta v}^2}{\overline{v}^2(1+2\cos^2(\theta-\gamma))+2\overline{\Delta v}^2} \right) A(D,\, d,\, \gamma)$$
$$+ \left(\frac{\overline{v}^2\, \sin^2(\theta-\gamma)+\frac{1}{2}\overline{\Delta v}^2}{\overline{v}^2(1+2\, \cos^2(\theta-\gamma))+2\overline{\Delta v}^2} \right) B(D,\, d,\, \gamma)$$
$$+ \left(2\frac{\overline{v}^2\, \sin(\theta-\gamma)\cos(\theta-\gamma)}{\overline{v}^2(1+2\, \cos^2(\theta-\gamma))+2\overline{\Delta v}^2} \right) C(D,\, d,\, \gamma)$$

$A(D,\, d,\, \gamma)$, $B(D,\, d,\, \gamma)$ and $C(D,\, d,\, \gamma)$ are integral functions expressed in Appendix 2. As they do not possess analytical solutions they have to be computed numerically. Table 2 gives a set of solutions for pupils of 12 cm diameter separated by 20 cm.

Table 2. The parameters of the covariance, $A(D,\, d,\, \gamma)$, $B(D,\, d,\, \gamma)$ and $C(D,\, d,\, \gamma)$: a set of numerical solutions of the integral functions expressed in Appendix 2 for pupil diameters of 12 cm, 20 cm apart.

$\gamma°$	$A(D,d,\gamma)$	$B(D,d,\gamma)$	$C(D,d,\gamma)$
0	-0.150	-0.119	0
30	-0.199	-0.046	-0.152
60	-0.033	0.046	-0.196
90	-0.316	-0.119	0
120	-0.033	0.046	0.196
150	-0.199	-0.046	0.152
180	-0.150	-0.119	0

The assumption of the kinematic model presented in Fig. 1 are multiple and thin moving atmospheric layers with inner frozen turbulence, near field approximation, and Kolmogorov inertial law for the turbulence spectrum.

Because a physical interpretation concerning the theory of the measurement is easier when neglecting the covariance term in the structure function equation, the first results presented in § 5 are computed using this simplification. An error is generated on the estimate of the measured layers velocities and of the θ direction, respectively of about 4% and plus or minus 15 Degrees.

4.2. New instrumental set-up

The share of the high frequency image wander is significant in the structure function $D_{\frac{\partial \alpha}{\partial t},\gamma}$. Because the classical seeing monitor detector controller has a too low sampling rate for our purpose (the minimum time between two read-outs of 20x20 pixels subimages is limited to 64 ms), an optical adaptor has been designed to increase the effective image acquisition rate. A scanning device constituted by a tilt mirror mounted on a galvanometer is installed in the afocal beam after the roof prism of the seeing monitor, between the two usual lenses: collimator and CCD objective. When observing with the new set-up, the tilting mirror driven by a staircase signal shown in Fig. 3 moves the dual star image across the CCD detector after each exposure in a direction perpendicular to the subpupil separation (Fig. 2). Several dual images are therefore formed in the image plane detector, their temporal separation is directed by the step period. Their exposure time is determined by the aspect ratio of a chopping wheel occulting the light when the scanning mirror moves from one step to the other. The chopper also permits to avoid blurring of the individual stellar images caused by the finite impulse response time of the scanner (typically 0.4 milliseconds for small rotation angles). The shutter mentioned in § 3.2 is triggered by the scanning signal with an exposure time adjusted to the transit time of the beams across the CCD.

As a result, by means of this optical oscilloscope, two dimensional frames are obtained containing several pairs of stellar images with submillisecond exposure time (~ 0.7 ms) and a sampling rate of up to 500 Hz. The frame processing is done on line, it includes the detection of the stellar images and the determination of the position of their individual centroid. The differential image motion velocity is derived from the difference of the relative displacements of two adjacent pairs divided by their temporal separation.

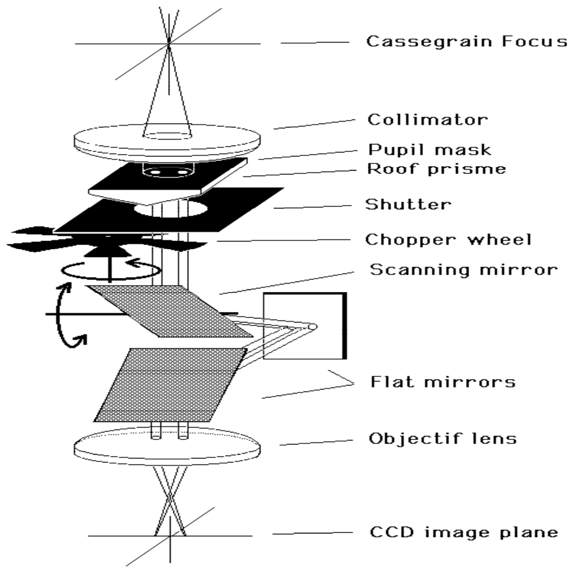

Fig. 2. Optical adaptor for the DIMM: a tilt mirror drives the dual star images across the CCD detector.

4.3. Instrumental limitations

The pupil sizes are necessarily different from those used in classical DIMM operation. Because the exposure time per dual

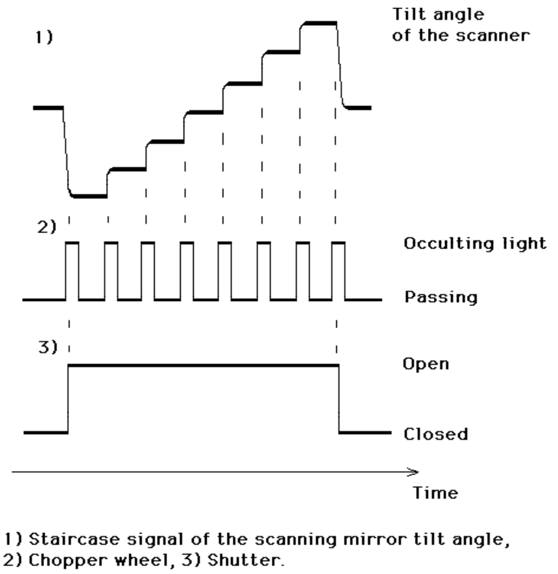

Fig. 3. Input signals used to obtain CCD frames containing several pairs of stellar images with submillisecond exposure time ($\sim$ 0.7 ms) separated by 2 ms.

images is much shorter, photometric considerations impose an increase of the aperture diameter. Secondly, the choice of the pupil size determines the maximum wavefront velocity that can be measured without time-filtering effect. The time spectrum of the angle of arrival velocity has been previously analyzed (Lopez 1992). The condition for sampling the full bandwidth at Shannon frequency depends on the atmospheric conditions:

$$sup(\frac{\nu r_0}{2}, \frac{\nu D}{2}) > sup(\overline{v}, \overline{\Delta v}) \tag{14}$$

where D is the pupil diameter, ν the sampling rate of the system. For the 12 cm pupil diameter which are in use when observing temporal-coherence with the modified seeing monitor and for a sampling frequency of 500 Hz delivered by the adaptor, the maximum horizontal wavefront velocity properly measured is about 30 m/s.
The remaining uncertainty is caused by the error on the determination of the centroid position which generates a noise of variance $N^2_{\frac{\partial\alpha}{\partial t}}$ on the derived image velocity variance. $N_{\frac{\partial\alpha}{\partial t}}$ depends slightly on the direction γ, however its mean value can be estimated from the noise N^2_α on the position measurements given in Eq. (10) by:

$$\begin{aligned} N^2_{\frac{\partial\alpha}{\partial t}} &\approx 2\nu^2 N^2_\alpha \\ &\approx 10^{-7}\ rd^2.s^{-2}\ for\, \nu = 500\, Hz. \end{aligned} \tag{15}$$

Measurements of this quantity realized with an artificial source located at the Cassegrain focus lead to the following more realistic value including the effect of the tilt mirror and chopper wheel. The noise term averaged over all directions of measurement and for ν = 500 Hz is given as a mean variance $\pm$ the rms of fluctuations around the mean:

$$N^2_{\frac{\partial\alpha}{\partial t}} = (1.25 \pm 0.03)\, 10^{-7}\ rd^2.s^{-2}. \tag{16}$$

The noise term is statistically independent of the tilt velocity and can be subtracted out from the variance in every direction of measurement independently. $N^2_{\gamma,\frac{\partial\alpha}{\partial t}}$ is the sum of a systematic error and of a random quantity $\delta N^2_{\frac{\partial\alpha}{\partial t}}$ independent of the direction γ. After subtraction of the systematic error, $\delta N_{\frac{\partial\alpha}{\partial t}}$ sets the signal to noise ratio on the computed velocity variance in the direction γ:

$$(\frac{S}{N})_\gamma = \sqrt{\frac{D_{\gamma,\frac{\partial\alpha}{\partial t}}}{\delta N^2_{\frac{\partial\alpha}{\partial t}}}} \tag{17}$$

and thus depends on r_0, $\overline{\Delta v}$, $\overline{v}$, θ, D, d and γ. We take the particular case of the longitudinal structure function with $\theta = \pi/4$. The structure function can be roughly simplified to:

$$D_{\frac{\partial\alpha}{\delta t}} = 0.512\,\lambda^2\, r_0^{-5/3}\, D^{-7/3}(\overline{v}^2 + \overline{\Delta v}^2) \tag{18}$$

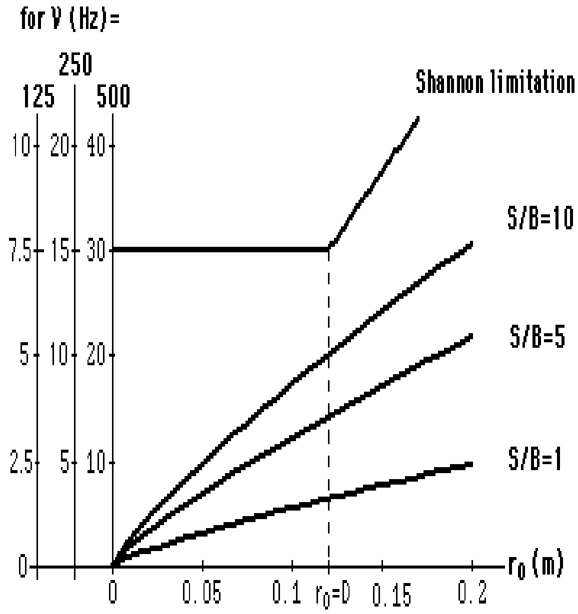

Fig. 4. Analysis of the trade-off between Signal to Noise ratio and Shannon limitation for different conditions of spatio-temporal coherence according to Eq. (14) with 12 cm diameter pupils.

Signal to noise ratio and Shannon limitation relations, both depending on r_0, $\overline{\Delta v}$, $\overline{v}$, are plotted together in Fig. 4. This diagram allows to determine the sampling frequency at which $\overline{\Delta v}$, $\overline{v}$, versus r_0 are correctly measured: decreasing the image motion acquisition frequency improves the signal to noise ratio but, on the other hand the Shannon theorem limits the maximum velocity properly measured. Therefore the acquisition frequency must be adapted in real time to the turbulent conditions. The sampling rate of the coherence monitor is changed accordingly by recomputing the variance on the same time series with a time lag increasing from one to four samples. This method simulates a frequency variation from 500 Hz to 125 Hz, among which the result with the highest signal to noise ratio verifying Eq. 14 is chosen.

5. First results of measurements made at La Silla

The modified differential image motion monitor is installed on a tower 5 meters above ground at the La Silla Observatory close to the Schmidt telescope. The data presented hereafter correspond to 7 nights of continuous monitoring realized in coordination with the first technical run of the Come-On-Plus adaptive optics system installed on the 3.6 m telescope in December 1992 (Hubin et al. 1992). The first statistical measures on turbulent layers allowingthe wavefront time characteristics to be determined were in fact obtained with the same instrument at Paranal during the PARSCA Campaign in March 92 (Sarazin 1992), but with a degraded accuracy. The spatiotemporal parameters of the atmosphere, namely seeing, scintillation, average and dispersion velocities, and average direction were monitored each night at a rate of one estimate every 8 mn on the basis of 200 image pairs. The output rate of the coherence monitor is currently limited by the computing power installed and should be closer to 2 mn for a correct sampling of atmospheric changes. Figure 5 shows a complete night of measurement of the kinematic parameters of the turbulent atmosphere, illustrating the partial decorrelation between the velocity of the wavefront and its spatial coherence. Figure 6 presents histograms displaying the data on r_0, $\overline{\Delta v}$, $\overline{v}$ and on the speckle life time.

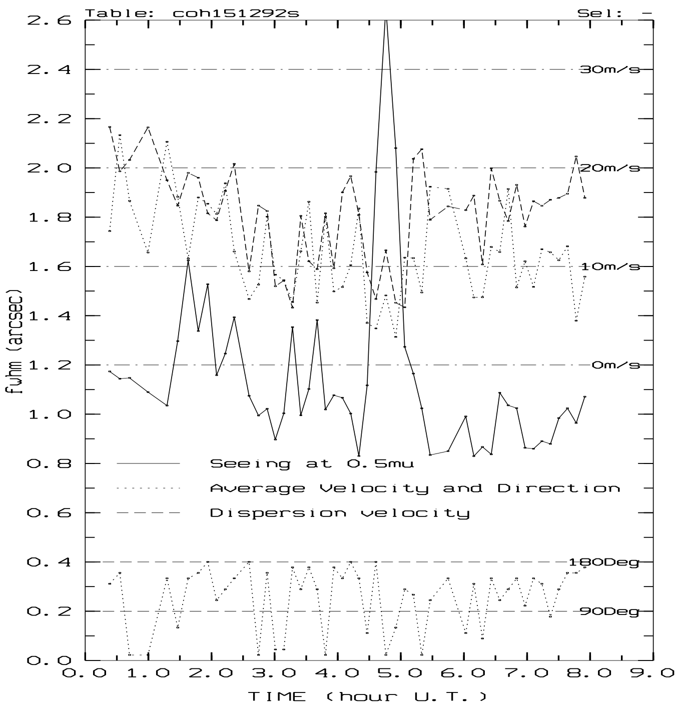

Fig. 5. A complete night of measurements of the kinematic parameters of the turbulent atmosphere on December 15, 1992 at La Silla. The average direction of the tilt has a 180 degree symmetry.

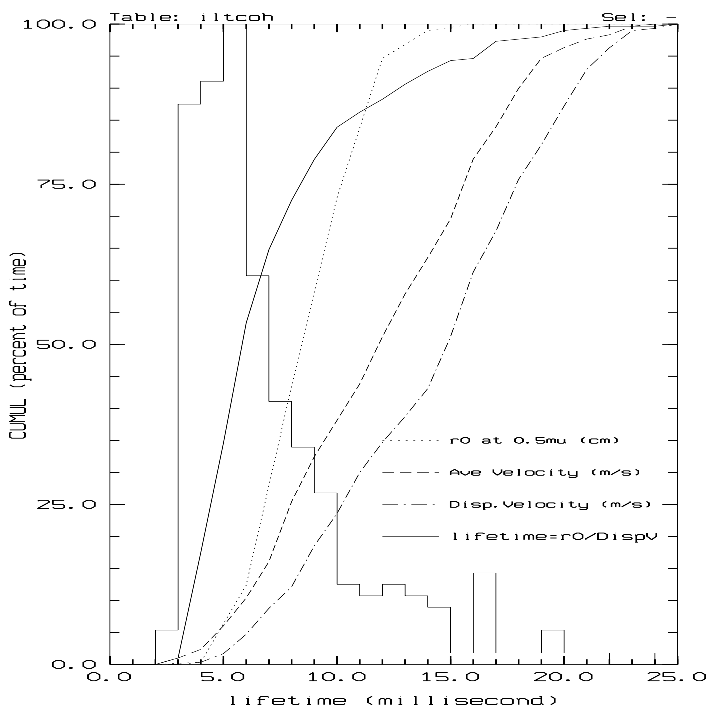

Fig. 6. Histograms of τ and probability distribution corresponding to 1 week of data on r_0, $\overline{\Delta v}$, $\overline{v}$ and on the speckle life time as defined in Eq. (4).

Acknowledgements: This work was supported by ESO as a part of the VLT Astronomical Weather Station (AWS) instrumentation package, following a suggestion by J. Beckers. The first possible observations were obtained thanks to the continuous technical help of R. Castillo, M. Morhinweg and G. Timmermann from La Silla TRS department, of J. Navarrete from VLT Site and Building Services at Paranal, and of the DIMM operators at Cerro Paranal.
Thanks also to technical help of Y. Bresson and P. Antonelli from OCA Observatory. We wish also thank J. Gay, P. Léna, D. Mékarnia, Ch. Perrier and F. Roddier for helpful comments and encouraging discussions. Thanks also J. Colin for his help in the preparation of the paper

Appendix 1

The mean velocity of wind for turbulent layers, useful to express the optimum exposure time for Michelson Interferometry is given by

$$v^* = \Big[\frac{\int_0^\infty \mid v(h) \mid^{5/3} C_n^2(h)dh}{\int_0^\infty C_n^2(h)dh}\Big]^{3/5}$$

which ranges between

$$\frac{\int_0^\infty v(h)\, C_n^2(h)dh}{\int_0^\infty C_n^2(h)dh} \leq v^* \leq \Big[\frac{\int_0^\infty \mid v(h) \mid^2 C_n^2(h)dh}{\int_0^\infty C_n^2(h)dh}\Big]^{1/2}$$

According to the presented method that allows the measures of $\overline{\Delta v}$ and $\overline{v}$ the inequality is

$$\overline{v} \leq v^* \leq [\overline{v}^2 + \overline{\Delta v}^2]^{1/2}$$

Appendix 2

$$A(D,\, d,\, \gamma) = 1.431\, D^{1/3} \iint_{-\infty}^{+\infty} f_x^4\, f^{-17/3}\, J_1^2(\pi D f)$$
$$\cos(2\pi\, \mu(f_x \cos\gamma + f_y\, \sin\gamma))df_x\, df_y$$

$$B(D,\, d,\, \gamma) = 1.431\, D^{1/3} \iint_{-\infty}^{+\infty} f_x^2 f_y^2 f^{-17/3}\, J_1^2(\pi D f)$$
$$\cos(2\pi\mu(f_x \cos\gamma + f_y\, \sin\gamma))df_x df_y$$

$$C(D,\, d,\, \gamma) = 1.431\, D^{1/3} \iint_{-\infty}^{+\infty} f_x^3 f_y f^{-17/3}\, J_1^2(\pi D f)$$
$$\cos(2\pi\mu(f_x \cos\gamma + f_y\, \sin\gamma))df_x df_y$$

with $f = (f_x^2 + f_y^2)^{1/2}$
where f_x and f_y are spatial frequencies, μ is the subpupil separation, J_1 is the first order Bessel function.

References

M. Abitbol, N. Subovitch, N. Ben-Yosef; *A method for the investigation of the spatio-temporal atmospherically perturbed wavefronts at high temporal frequency*; I.C.O. Top. Meeting on Atmospheric, Volume and Surface Scattering and Propagation; Florence, Italy, Aug. 27-30, 1991.

C. Aime, J. Borgnino, F. Martin, R. Petrov, G. Ricort, S. Kadiri; *Contribution to the space-time study of stellar speckle patterns*; JOSA A, Vol.3, p1001, July 86.

M. M. Colavita, M. Shao, D. H. Staelin; Atmospheric phase measurements with the Mark III stellar interferometer; Applied Optics, Vol.26 n^o:19, 1 Oct. 87.

D.L. Fried; *Differential angle of arrival: Theory, evaluation and measurement feasibility*; Radio Science, **10** No:1, 71-76, January 1975.

N. Hubin et Al. ;*New adaptive optics prototype system for the ESO 3.6 m telescope: Come-On-Plus*; ESO preprint **48**, Sep. 1992, S.P.I.E. 1780.

M.B. Jorgenson, G.J.M. Aitken, E.K. Hege; *Evidence of a chaotic attractor in star-wander data*; Optics Letters **16**, 2, 1991.

B. Lopez, M. Sarazin; *Optimum exposure times for interferometry*; Proc. ESO-Conf. on High Resolution Imaging by Interferometry II; Garching, Oct 14-18, 1991.

B. Lopez; *How to monitor exposure times for high resolution imaging modes?*; A&A 253, 635-640 (1992).

M. Müller, G. Baier, S. Helm, G. Weigelt;*Optical Parameters of the Atmosphere*; Proc. NOAO-ESO conf. on: High-resolution imaging by Interferometry, Garching, 15-18 March 88, ed. F. Merkle.

F. Roddier; *The effect of atmospheric turbulence in optical astronomy*; E.Wolf ed., Progress in Optics Vol. XIX, 1981, p. 281.

F. Roddier, J. M. Gilli, G. Lund; *On the origin of speckle boiling ant its effects in stellar speckle interferometry*; J. Optics, **13**, 5, 1982.

F. Roddier, P. Léna; *Long Baseline Interferometry with large ground-based telescopes operating at optical wavelengths*; J. Optics, **15** 4, 171-182, 1984.

M. Sarazin, F. Roddier; *The E.S.O Differential Image Motion Monitor*; A&A 227, 294-300 (1990).

M. Sarazin; *PARSCA 92: the Paranal Seeing Campaign*; The Messenger **68** June 92.

R.J. Scaddan, J.G. Walker; *Statistics of stellar speckle patterns*; Applied Optics **17**, 23, 1978.

D.B. Soules, J.J. Drexler, A.H. Waldie, J.A. Qualtrough, F.D. Eaton, W.A. Peterson, J.R. Hines; *Temporal characteristics of turbulence-induced image motion*;Tech. Sympos. on Aerospace Sensing, SPIE **1115** (1989).

J. Vernin, G. Weigelt, J-L. Caccia, M. Müller; *Speckle lifetime and isoplanicity determinations: direct measurements and derivation from turbulence and wind profiles*; A&A 243, 553-558 (1991).

This article was processed by the author using Springer-Verlag LaTeX A&A style file 1990.